Solar salt encapsulated into 3D printed activated carbon/alumina supports for thermal energy storage applications

Irene Díaz-Herrezuelo, Quentin Falcoz, Audrey Soum-Glaude, Manuel Belmonte

Open Ceramics 19 (2024) 100648

Contents lists available at ScienceDirect

Open Ceramics

journal homepage: www.sciencedirect.com/journal/open-ceramics

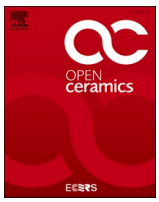

Solar salt encapsulated into 3D printed activated carbon/alumina supports for thermal energy storage applications

Irene Díaz-Herrezuelo [a], Quentin Falcoz [b,c], Audrey Soum-Glaude [b], Manuel Belmonte [a,*]

[a] Institute of Ceramics and Glass (ICV, CSIC), Kelsen 5, 28049, Madrid, Spain
[b] Laboratory of Processes, Materials and Solar Energy (PROMES-CNRS UPR 8521), 7 rue du Four Solaire, 66120, Font-Romeu Odeillo, France
[c] University of Perpignan Via Domitia (UPVD), 52 avenue Paul Alduy, 66860, Perpignan, France

ARTICLE INFO

Handling Editor: P Colombo

Keywords:
Thermal energy storage
Solar salt
Additive manufacturing
Porous supports
Alumina
Carbon

ABSTRACT

The encapsulation of phase change materials (PCMs) into additive manufactured porous supports is attracting great interest for developing thermal energy storage (TES) materials with improved energy performance. Here, highly porous (86 %) self-supported 3D activated carbon/alumina supports are fabricated by direct ink writing (DIW) and, then, infiltrated with solar salt, a highly corrosive PCM with a melting temperature around 220 °C commonly employed in concentrated solar power plants. This novel, robust, chemically compatible, and lightweight infiltrated 3DTES exhibits good thermal energy storage efficiency (70 %) and thermal stability, high energy storage density (381 J g^{-1}), and avoids the liquid leakage of the molten salt. Besides, the 3D activated carbon/alumina support promotes a better ability to absorb solar energy (79 %) and enhances the thermal conductivity of the solar salt (up to 64 %). These results validate the use of DIW for manufacturing innovative TES with an enhanced energy storage behaviour.

1. Introduction

The solar salt, an inorganic mixture of sodium and potassium nitrates, is a liquid-solid phase change material (PCM) commonly employed as thermal energy storage (TES) material in concentrated solar power (CSP) applications. This salt stands out as PCM due to its good energy storage performance and low cost [1]. However, as any PCM, it presents some drawbacks that limit the range of their potential applications, such as the low thermal conductivity that abruptly decreases the heat transfer rate and, hence, the charging-discharging ability, also leading to large temperature gradients; and the liquid leakage in the molten state that substantially reduces the energy storage efficiency and avoids the thermal regulation of waste heat [2]. One of the main approaches to mitigate these deficiencies is the development of form-stable composite PCM (FSPCM) by encapsulating the PCM into thermally conductive porous supporting materials, including metal, polymer, ceramic and carbon-based foams and aerogels [3–5], which present high specific surface area and can incorporate large PCM contents, preventing the liquid leakage in the molten state. Taking into account the corrosiveness of the solar salt and its melting temperature (~220 °C), metal and organic porous structures are not suitable for encapsulating this PCM. On the other hand, carbon-based (graphene, carbon nanotubes, graphite, carbon black) foams and aerogels have mostly been employed to encapsulate organic PCMs (paraffin, fatty acids, polyethylene glycol …) [3–5], although few works have reported the infiltration of these carbon-based porous structures with high temperature and corrosive inorganic salts. In this way, graphite foams have been infiltrated with magnesium chloride [6,7], a blend of alkali and alkaline chloride salts [8,9], or with sodium nitrate [10], leading to substantial improvements in the thermal conductivity and leakage resistance of the PCM. However, the encapsulation capacities of the PCM were in the range of 70–80 %, which reduced the enthalpy of fusion, and, in addition, the mechanical stability of the infiltrated carbon foams was low, compromising their long-term energy storage capabilities [5]. Ceramic foams based on alumina (Al_2O_3) have also been employed as porous supports for encapsulating sodium sulphate and sodium chloride salts [11]. Although these FSPCM presented encapsulation capacities below 40 %, they exhibited high compressive strength and thermal conductivity values (up to 100 MPa and 6.4 W m^{-1} K^{-1}, respectively). Finally, alumina and graphite have been combined to produce porous foams, which have subsequently been infiltrated with a low temperature organic PCM such as paraffin [12,13]. This FSPCM reached maximum encapsulation capacities of 66 % with no liquid leakage, and the thermal conductivity of the PCM increased due to the interconnected porous

* Corresponding author.
E-mail address: mbelmonte@icv.csic.es (M. Belmonte).

https://doi.org/10.1016/j.oceram.2024.100648
Received 7 June 2024; Received in revised form 19 July 2024; Accepted 22 July 2024
Available online 26 July 2024

structure of the foam. However, the energy efficiency was relatively low (60 %) [12].

Lately, a new class of TES based on the PCM infiltration of additive manufactured porous 3D structures (polymers, metals, cements and ceramics) has been proposed [14–16]. These cellular supports have attracted great attention because, as compared with foams, they exhibit higher strength-to-weight ratio, stiffness, and enhanced energy absorption, also allowing to design complex lattices for improving the heat transport. Once more, organic PCMs have been employed in the majority of the reported studies. In the case of molten salts, some of the present authors have recently developed 3DTES based on 3D printed clay supports infiltrated with molten sodium nitrate [16,17], which exhibited excellent energy storage performance and absence of liquid leakage. Taking into account the above considerations, in the current work, highly porous 3D patterned activated carbon/alumina (AC/Al_2O_3) structures have been manufactured by direct ink writing (also known as Robocasting) and, then, they have been infiltrated with molten solar salt. That combination of materials for the support has been selected with the aim to enhance its thermal conductivity and mechanical resistance. The thermal, mechanical and energy performance of the solar salt infiltrated on 3D AC/Al_2O_3 structures (labelled as 3DTES-SS) have been investigated.

2. Material and methods

2.1. Functionalization of AC powders

Charcoal activated powder (<100 nm particle size, Merck) was used as AC starting material. Considering the poor wettability of graphitic surfaces with molten salts [18], AC powders were previously functionalized to incorporate hydrophilic polar sites that should improve the wettability [19]. In this way, oxidized AC (AC_{ox}) was obtained by treating the pristine powders with nitric acid according to the procedure described below. First, 10 g of AC were gradually added to a flask containing 100 ml of concentrated nitric acid (65 % EPR), which was immersed in a cold-water bath (20 °C) for 40 min. Once the AC addition was concluded, the solution was heated at 80 °C for 4 h under reflux with magnetic stirring at 60 rpm. Then, it was cooled down to room temperature, filtrated and washed with distilled water few times to extract the AC_{ox}. Finally, the resulting black powder was fully dried at 100 °C for 14 h.

The characterization of pristine AC and AC_{ox} powders was carried out by different techniques (see Table S1 in the supplementary information). The specific surface area (S_{BET}) and external surface area (A_{EXT}) were measured by a TriStar 3000 Equipment (Micrometrics) using the Brunauer-Emmett-Teller (BET) method in nitrogen at a degassing temperature of 120 °C. The determination of carbon, oxygen, nitrogen and sulphur content was done using two analysers (LECO TC-500 for nitrogen and oxygen and LECO CS-200 for carbon and sulphur). As expected, the oxidation process slightly modified the surface characteristics of pristine AC, leading to a slight decrease (~13 %) in S_{BET} and A_{EXT}. In addition, the oxygen content considerably augmented in the chemically treated powders, from 7.7 wt% for AC to 27.1 wt% for AC_{ox}, which would promote the wettability with the molten salt. Thermogravimetric/differential thermal analysis (TGA/DTA, Q600, TA Instruments) tests were performed to investigate the thermal stability up to 1000 °C at a heating rate of 5 °C min^{-1} in air (Fig. S1). In this way, AC_{ox} presented a weight loss of 13.5 % from room temperature to 110 °C that would correspond to the evaporation of adsorbed water. In a second stage, the weight loss between 110 °C and 310 °C was 5.3 %, which would be related to the degradation of the functional groups attached to the powder surface. Finally, the weight loss for higher temperatures suddenly augmented due to the decomposition of AC, which fully finished at 620 °C.

2.2. Direct ink writing of AC_{ox}-boehmite supports

In order to develop the printable ink, first, a boehmite gel (AlO(OH)), selected as alumina precursor, was prepared mechanically stirring at 500 rpm for 90 min in an ice/water bath a Milli-Q water solution containing 41 wt% of boehmite powders (Dispal 11N7-80, SASOL, 220 nm particle size modified with 0.1 wt% of nitric acid). Then, the ink was obtained by successively mixing AC_{ox} powders and the boehmite gel, in a relation of 55:45 (in wt.%), and Milli-Q water. The ink was homogenized in a planetary centrifugal mixer (AR-250, Thinky Company) at 2000 rpm during 30 s, using silicon nitride balls as milling media. The final ink had a 41.3 wt% of solid content and the following composition (in weight): 22.7 % of AC_{ox}, 18.6 % of boehmite and 58.7 % of total water (14.9, 8.1 and 77.0 in vol%, respectively). The rheological properties of the ink, including the apparent viscosity (η) as a function of the shear rate ($\dot{\gamma}$), and the shear storage (G′) and loss (G″) moduli versus the shear stress (τ), were measured using a rheometer (CVO 100 D, Bohlin Instruments) with a cone-and-plate geometry (diameter: 40 mm; cone angle: 4°) at 25 °C in the 10^{-1}-10^{2} s^{-1} and 1-10^{4} Pa ranges, respectively.

Unframed cylindrical 3D supports of 16.2 mm in diameter and 5.3 mm in height were computer designed with a CAD software (RoboCAD 4.2, 3-D Inks LLC) to produce 3D cellular structures formed by eight layers, each one being orthogonal respect to the adjacent one, and containing a linear array of seven parallel filaments in the X–Y plane. The inks were extruded with a three-axis robocasting system (A3200, 3-D Inks LLC) at a constant speed of 10 mm s^{-1} at room temperature in air through a nozzle tip of 840 μm inner diameter (Precision Tips, EFD Inc.). The as-printed 3D AC_{ox}/boehmite scaffolds were heat treated at 1300 °C for 5 min in argon atmosphere using a pressureless spark plasma sintering furnace (SPS-510CE, SPS Syntex Inc.) to transform the boehmite phase into a crystalline alumina phase. The aim of this process was to reach a proper mechanical and corrosive resistance of the AC_{ox}/Al_2O_3 scaffolds during the subsequent molten solar salt infiltration process. Besides, the thermal conditions were selected to keep AC_{ox} invariable into the 3D structure.

As-printed and heat-treated scaffolds were analysed by optical stereomicroscopy (Nikon SMZ1000). The crystalline phases were determined using an X-ray diffractometer (XRD, Bruker D8 Advance) with a Linx Eye detector, and employing CuKα radiation in the 2θ range between 10° and 80°. The distinct density and porosity parameters of the heat-treated scaffolds were determined. In this way, geometrical density (ρ_{geo}) was assessed from the weight (W) and volume (V) of the scaffolds. Bulk density (ρ_{bulk}) was calculated with the Archimedes' method by measuring the dry weight (W), immersed weight (W_{DIW}) and soaked weight (W_S) of the 3D structures using the following equation: $\rho_{bulk} = W/(W_S-W_{DIW})$. Total porosity ($\pi_{total}$) was assessed using the expression: $\pi_{total} = 100 - (\rho_{geo} \times 100)/\rho_{th}$), considering a theoretical density (ρ_{th}) of 2.95 g cm^{-3}, which was calculated from the contribution to the total solid content of the individual theoretical density for each material after the heat treatment, i.e., 2.10 g cm^{-3} for AC_{ox} and 3.98 g cm^{-3} for α-Al_2O_3. Rod porosity (π_{rod}), that corresponds to the AC_{ox}/Al_2O_3 filaments, was estimated from the equation: $\pi_{rod} = 100 - [(\rho_{bulk} \times 100)/\rho_{th}]$; whereas 3D porosity ($\pi_{3D}$), referred to the open channels of the CAD design, was assessed as follows: $\pi_{3D} = \pi_{total} - [\pi_{rod} \times (V_{3Dstrut}/V)]$, where $V_{3Dstrut}$ is calculated as W/ρ_{bulk}.

2.3. Solar salt infiltration into 3D AC_{ox}/Al_2O_3 scaffolds

$NaNO_3$ and KNO_3 (purity ≥99.0 %) were employed as raw materials to formulate the binary mixture of solar salt in a 60:40 mass ratio (64:36 mol%). In this way, 120 g of $NaNO_3$ and 80 g of KNO_3 were mechanically mixed under dry conditions. The mixture was placed into an alumina crucible and heated up to 270 °C in air until reaching the complete melting (222 °C) of the powder. Afterwards, the molten solar salt was poured over a brass plate for fast cooling. Finally, the solidified material was milled in a mortar. For the infiltration process, ~9 g of the milled

solar salt were added to an alumina crucible and melted up to 270 °C in air. Subsequently, the 3D support was completely introduced into the molten salt for 20 min to ensure a high PCM infiltration into the scaffold. Thereafter, the specimen was removed from the liquid and cooled down to room temperature in air conditions.

The PCM encapsulation capacity (η_e) into the AC_{ox}/Al_2O_3 scaffold was calculated with this equation: η_e (%) = 100 x ($W_{PCM} - W_{3D}$)/W_{PCM}, where W_{PCM} is the weight of the 3DTES and W_{3D} is the weight of the 3D AC_{ox}/Al_2O_3 support before the infiltration step. To analyse the PCM leakage of the supporting material, ten consecutive drains were performed at 270 °C for 20 min in air, measuring the weight after each drain. 3DTES were microstructurally characterized by optical stereomicroscopy, field emission scanning electron microscopy (FESEM, Hitachi S-4700) and X-ray computed tomography (CT, CT-SCAN-XT H-160, Nikon). XRD tests were also carried out to study the chemical stability of the molten salt and the 3D support after the infiltration process.

Differential scanning calorimetry (DSC, Discovery DSC, TA Instruments) was employed to obtain the melting (T_f) and solidifying (T_s) onset temperatures, and the enthalpies of fusion (ΔH_f) and solidification (ΔH_s) in the 25–270 °C temperature range, using a heating/cooling rate of 5 °C min^{-1} and nitrogen as purge gas. The thermal energy storage efficiency (E_s) was calculated with the following equation: E_s (%) = $100\ x\ (\Delta H_{f,3D} + \Delta H_{s,3D})/(\Delta H_{f,PCM} + \Delta H_{s,PCM})$, where $\Delta H_{f,3D}$ and $\Delta H_{s,3D}$ are the enthalpies of fusion and solidification of the 3DTES, respectively, and $\Delta H_{f,PCM}$ and $\Delta H_{s,PCM}$ refer to the corresponding enthalpies of the pure solar salt. Besides, the thermal stability of the 3DTES was analysed by DSC running fourteen thermal cycles in the temperature range of 70–270 °C.

The specific heat (C_p) as a function of the temperature was measured by DSC up to 270 °C with a heating/cooling rate of 10 °C min^{-1}. The energy storage density (Q), sum of the sensible heat storage contribution -which depends on C_p in the solid state and after the complete melting of the PCM-plus the latent heat storage contribution -related to the solid-liquid phase transition, i.e., ΔH_f, was assessed from the following equation:

$$Q = \int_{T_i}^{T_f} C_{ps} \cdot dT + \Delta H_f + \int_{T_f}^{T_e} C_{pl} \cdot dT \quad (1)$$

where T_i and T_e are the initial and final temperatures, respectively, C_{ps} is the specific heat in the solid state between T_i and T_f, and C_{pl} is the specific heat in the molten state between T_f and T_e. Both C_p were assessed by integrating the plot in the corresponding temperature intervals.

The thermal conductivity (k_T) evolution of the PCM and 3DTES with the temperature, from room temperature to 180 °C, was calculated from the equation: k_T (T) = α (T) · ρ · C_p (T), where ρ is the density of the 3DTES and α is the thermal diffusivity measured by the laser flash method (LFA, Thermaflash 2200, Holometrix Netzsch). For LFA tests, 3DTES were cut and ground to achieve specimens with a final dimension of 8.8 x 8.8 x 2.0 mm^3. They were gold and then graphite coated and tested in argon atmosphere.

Optical reflectance spectra were obtained with two spectrophotometers. A two-beam scan spectrophotometer (PerkinElmer Lambda 950) equipped with a 150 mm diameter integrating sphere for the hemispherical reflectance measurements was employed for the 0.25–2.5 μm wavelength region (UV/Vis/NIR). Cylindrical specimens of 20 mm in diameter and 12 mm in height were prepared to achieve an illuminated area on the specimens of 12 x 4.5 mm^2. A SOC-100 HDR reflectometer (Surface Optics Corporation) equipped with 2π gold coated imaging hemi ellipsoid for the hemispherical directional reflectance measurements was used to attain the reflectance spectra in the 1.25–25.0 μm wavelength interval. Same cylindrical specimens were tested to ensure an illuminated spot of 12 mm in diameter. The solar absorptance (α_s) can be obtained from the spectral reflectance (opaque materials, no transmission) by:

$$\alpha_s = \frac{\int [1 - R(\lambda)] \cdot G(\lambda) \cdot d\lambda}{\int G(\lambda) \cdot d\lambda} \quad (2)$$

where R(λ) is the spectral reflectance and G(λ) is the standard solar irradiance spectrum (ASTM G173-03 a.m.1.5 Direct + circumsolar Reference Spectrum [20]). The limits for the integration are 0.28–4 μm. The thermal emittance ε(T) of 3DTES-SS has also been calculated by using the following equation:

$$\varepsilon(T) = \frac{\int [1 - R(\lambda)] \cdot M_\lambda^0(\lambda, T) \cdot d\lambda}{\int M_\lambda^0(\lambda, T) \cdot d\lambda} \quad (3)$$

where M_λ^0 (λ,T) is the blackbody spectrum at a temperature T, which is derived from Plank's law (M_λ^0 (λ,T) = (2·π·h·c^2/λ^5) x (1/(exp(h·c/λ·k_B·T) - 1)) [21]. The limits for the integration are 0.25–25 μm.

The compressive strength (σ_c) of 3DTES-SS was calculated using two compression testing machines (ZwickiLine Z5.0 TS, Zwick-Roell and EM2/200/FR, Microtest S.A., with 5 kN and 25 kN load cells, respectively). A displacement rate of 0.5 mm min^{-1} was employed until the 3D structures collapsed. For comparison purposes, σ_c of AC_{ox}/Al_2O_3 supports was also calculated using a 5 kN load cell. Top/bottom faces of all specimens were previously ground to ensure a homogeneous contact with the compression platens. At least four AC_{ox}/Al_2O_3 and 3DTES-SS specimens were tested.

3. Results and discussion

3.1. Manufacturing of 3D AC_{ox}/Al_2O_3 supports

The rheological behaviour of the AC_{ox}/boehmite ink is presented in Fig. 1. As it can be seen, the ink exhibits a pseudoplastic performance,

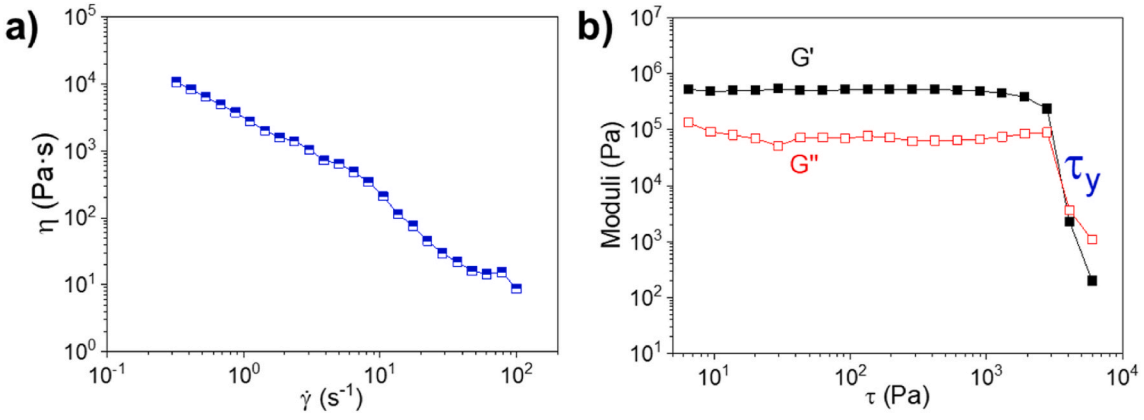

Fig. 1. Rheological characterization of the AC_{ox}/boehmite ink. a) Apparent viscosity (η) as a function of the shear rate ($\dot{\gamma}$) and b) shear storage (G′, full symbols) and loss (G″, empty symbols) moduli versus the shear stress (τ). The yield stress (τ_y) is also pointed.

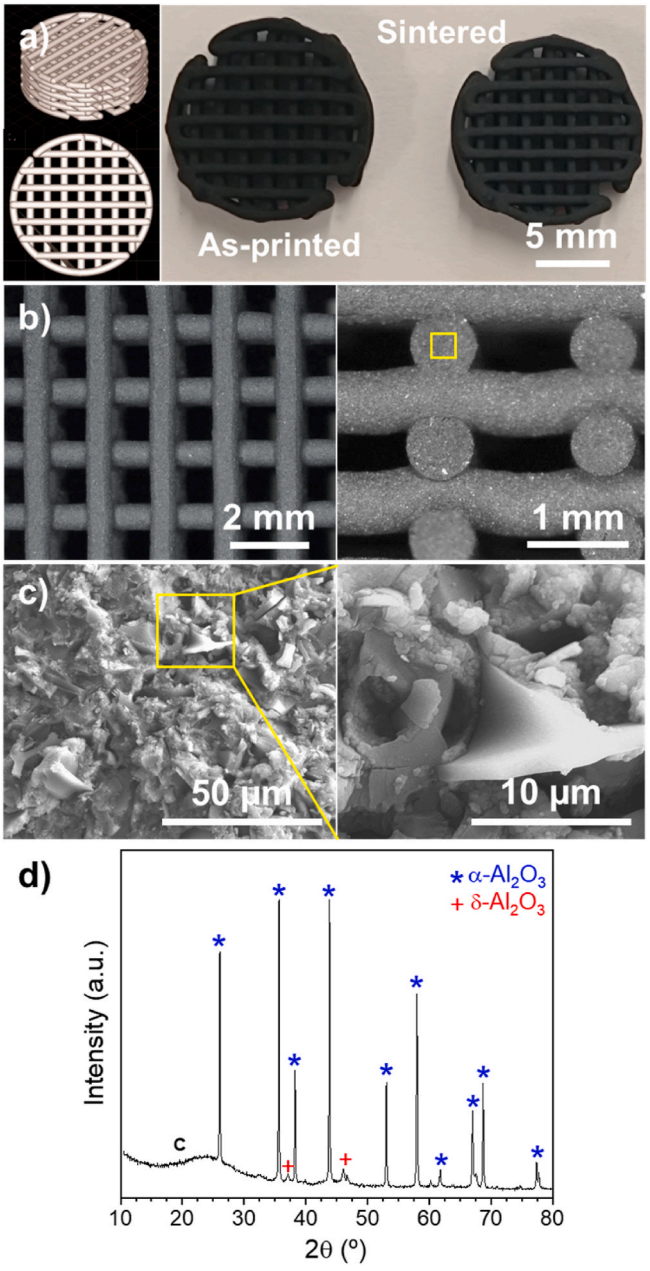

Fig. 2. 3D printed AC_{ox}/Al_2O_3 structures. a) Iso- and top-views of the CAD models (left column) and optical images of the as-printed and sintered 3D supports. b) Top (left) and cross-section (right) views of the 3D AC_{ox}/Al_2O_3 structures. c) SEM micrograph (left) at the centre of the rod corresponding to the zone enclosed in (b). The right-hand side image is a detail at high magnification of the marked square. d) XRD spectrum of the 3D supports after the sintering process.

confirmed by a decrease of η in about three orders of magnitude as $\dot{\gamma}$ augmented within the 10^{-1}-10^{2} s^{-1} interval (Fig. 1a). This response would support the printability of the developed ink and would also allow keeping the filamentary shape of the extruded rods. In addition, the shear moduli plot (Fig. 1b) shows that G′ reached a high and constant value (~5×10^5 Pa) above G'' (~8×10^4 Pa) until crossing at the yield stress (τ_y) of ~3.6×10^3 Pa, which would favour the building of robust self-supported 3D architectures.

Table 1
Geometrical density (ρ_{geo}), bulk density (ρ_{bulk}), total porosity (π_{total}), 3D porosity (π_{3D}) and rod porosity (π_{rod}) for 3D AC_{ox}/Al_2O_3 structures.

ρ_{geo} (g cm^{-3})	ρ_{bulk} (g cm^{-3})	π_{total} (vol%)	π_{3D} (vol%)	π_{rod} (vol%)
0.41 ± 0.01	0.91 ± 0.02	86.1 ± 0.2	54.9 ± 0.6	69.1 ± 0.5

The as-printed 3D AC_{ox}/boehmite scaffolds perfectly reproduced the CAD model with no evidence of damage after the selected sintering process (Fig. 2a and b), which also avoided the AC_{ox} degradation. The thermal treatment led to a slight shrinkage (~16 %) of the scaffold height and diameter (Fig. 2a), being the final dimensions of 13.5 mm in diameter and 4.5 mm in height. The patterned structure contained squared open channels of ~910 μm in side and a skeleton of straight filaments of ~710 μm in diameter (Fig. 2b). The densities and porosities of the sintered scaffolds are collected in Table 1. 3D supports were lightweight ($\rho_{geo} = 0.41$ g cm^{-3}) and highly porous ($\pi_{Total} = 86.1$ %) due to both the porosity of the open channels of the patterned design ($\pi_{3D} = 54.9$ %) and the porosity of the rods ($\pi_{rod} = 69.1$ %), which can be observed in Fig. 2c. These high porosity values would promote the infiltration of the molten solar salt into the 3D supports. The thermal treatment of the scaffolds at 1300 °C transformed the boehmite phase into the high mechanical resistant α-Al_2O_3 phase (Fig. 2d), with some traces of δ-Al_2O_3, leading to 3D AC_{ox}/Al_2O_3 structures. The broad region of the XRD spectrum in the 2θ region of 10-30° corresponds to the amorphous AC_{ox}.

3.2. 3DTES-SS

After the infiltration process, the encapsulation capacity of the solar salt into the 3D AC_{ox}/Al_2O_3 support reached a value of 75.6 % (in weight), which is higher than that attained for graphite/alumina foams infiltrated with paraffin ($\eta_e = 66$ %) [12,13] and comparable ($\eta_e =$ 70–80 %) to molten salts encapsulated into graphite foams [6–10] and 3D printed clays structures [16]. The optical inspection of the 3DTES-SS (Fig. 3a–c) apparently shows an excellent PCM infiltration grade into the printed skeleton, filling with the solar salt both the vertical (top view, Fig. 3b) and lateral (Fig. 3c) open channels. Additional CT analysis confirmed the complete infiltration inside the scaffolds with the solar salt (Fig. 3d–f). Besides, no cracks or damage of the 3D supports was observed. It is important to remark that, although the salt fully filled the scaffolds in the molten state, the differences in the PCM density between the crystalized (2.20 g cm^{-3}) and molten (1.93 g cm^{-3} at 270 °C) [22] states led to about 12 % decrease in its volume and, hence, the first top printed layer appeared empty after the solidification process (Fig. 3e).

The PCM leakage was investigated by running ten consecutive drain steps at 270 °C. After the last thermal cycle, η_e just decreased ~0.2 % from the initial value (Fig. 4a), evidencing that the molten salt kept encapsulated inside the 3D AC_{ox}/Al_2O_3 structure and the liquid leakage was avoided. This behaviour was favoured by the design of the highly porous 3D printed patterned architecture and the functionalization of AC.

The solid-liquid phase temperatures of the 3DTES-SS were established from DSC curves (Fig. 4b). During the heating process an endothermic broad peak with an onset temperature (T_f) of 220.7 °C (222.0 °C for the pure solar salt) was observed, which corresponded to the starting point of the melting process of the solar salt that ended at ~239 °C. Conversely, the salt initiated the crystallization (exothermic peaks) in

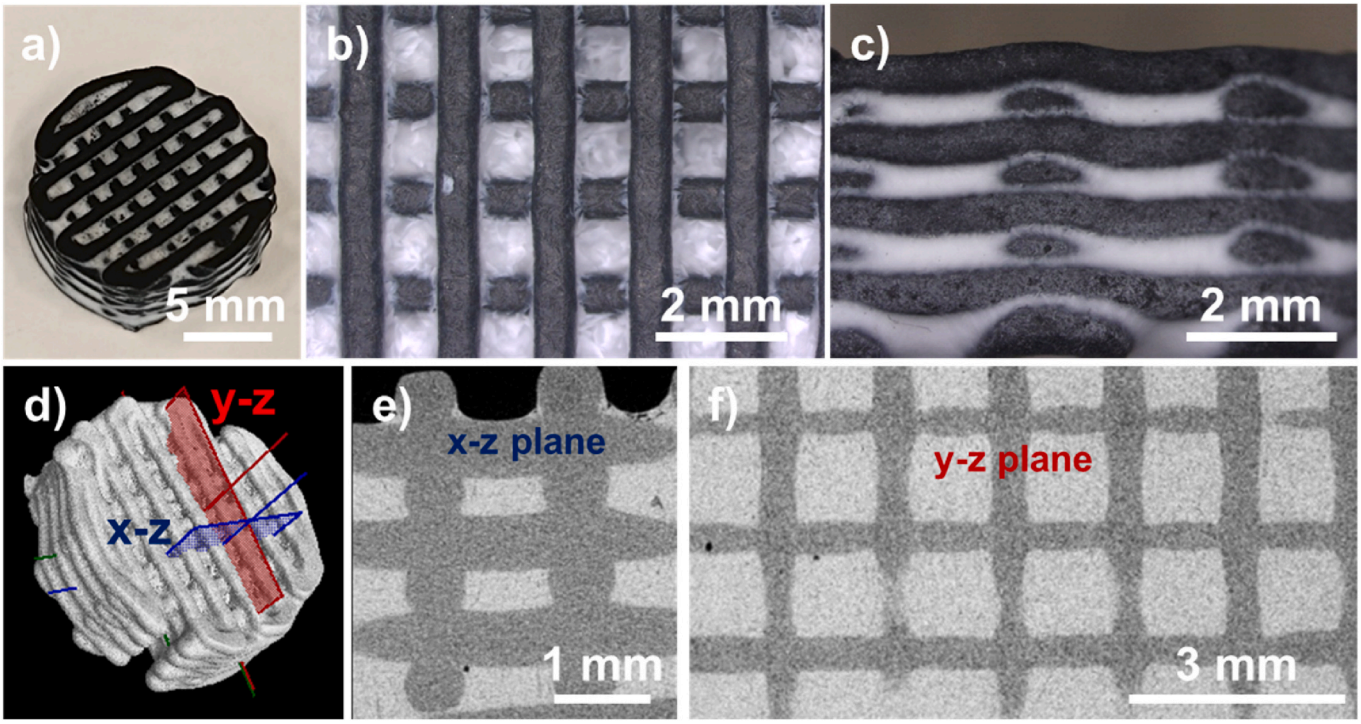

Fig. 3. Solar salt encapsulation into 3D AC_{ox}/Al_2O_3 supports. a-c) Optical images of the 3DTES-SS showing a general view of the scaffold infiltrated with the solar salt (a), which appears in white colour, and a detail of the top (b) and lateral (c) views of the 3DTES-SS where the vertical and lateral channels filled with the salt are clearly observed. d-f) CT images of the 3DTES-SS including an example of 2D x-z (e) and y-z (f) cutting planes. Light and dark grey colours correspond to the solar salt and AC_{ox}/Al_2O_3 filaments, respectively. (For interpretation of the references to colour in this figure legend, the reader is referred to the Web version of this article.)

the cooling process at an onset temperature (T_s) of 233.2 °C (236.7 °C for the pure solar salt), finishing the solidification of the PCM at ~217 °C. The enthalpies of fusion (ΔH_f) and solidification (ΔH_s) of the 3DTES-SS, determined from the corresponding endo- and exothermic peaks, were 78.0 J g^{-1} and 80.8 J g^{-1}, respectively (110.7 J g^{-1} and 115.1 J g^{-1} for the pure solar salt). Based on these results, it can be established a thermal energy storage efficiency (E_s) for the 3DTES-SS of 70.3 %. As it can be seen, T_f and T_s are slightly lower in the 3DTES-SS, a phenomenon that often occurs in FSPCM when the thermal conductivity of the supporting material is higher than that of the pure PCM. The remaining porosity in the infiltrated structure would also explain the 15 % decrease of the supercooling degree (ΔT_c), a parameter assessed from the difference between T_f and T_s, in the 3DTES-SS (ΔT_c = 12.5 °C vs 14.7 °C for the solar salt), as the porosity of the AC_{ox}/Al_2O_3 struts would promote the nucleation of the salt during the solidification process [23]. It should be pointed out that 3DTES-SS exhibited an outstanding thermal stability, confirmed by the negligible change of ΔH_f and ΔH_s along fourteen thermal cycles (Fig. 4c).

The thermal conductivity (k_T) evolution of the pure solar salt and 3DTES-SS with the temperature, from room temperature to 180 °C, is plotted in Fig. 4d. This parameter was calculated from the experimental C_p (Fig. S2a) and α (Fig. S2b) values. As it can be seen, when the solar salt is infiltrated into the 3DTES material k_T slightly augmented ~9 % at 25 °C, from 1.25 ± 0.02 W m^{-1} K^{-1} (molten salt) to 1.35 ± 0.13 W m^{-1} K^{-1} (3DTES-SS), which is due to the thermal contribution of the AC_{ox}/Al_2O_3 skeleton. For both materials, k_T progressively diminished with the temperature due to phonon-phonon scattering mechanisms, although the conductivity differences were enlarged and, at 180 °C, k_T for 3DTES-SS was about 64 % higher (1.17 ± 0.10 W m^{-1} K^{-1}) than for the solar salt (0.71 ± 0.01 W m^{-1} K^{-1}). Therefore, the thermal response close to the melting temperature of the PCM was clearly enhanced by the 3D supporting material.

Another important energy parameter is the energy storage density (Q) that allows estimating the heat storage potential of the TES. In the present case, a Q value of 381 J g^{-1} was attained for 3DTES-SS, considering a working temperature range between 25 and 270 °C, and specific heat values in the solid and liquid states of 1.20 J g^{-1} K^{-1} and 1.34 J g^{-1} K^{-1}, respectively. Besides, these TES materials presented a good ability to absorb in the solar spectrum range. Indeed, their solar absorptance (α_s) is 79 %, obtained by integrating the reflectivity spectrum in the 0.25–25 μm wavelength region (Fig. 5). This absorption performance is mainly due to the high solar absorptance of the 3D AC_{ox}/Al_2O_3 supports (α_s = 97 %), slightly larger than that reported for other ceramic absorbers tested for solar central receivers, such as Al_2O_3:SiO_2:Fe_2O_3:TiO_2 (α_s = 93 %) [24] or bauxite/Fe_2O_3/CuO (α_s = 94 %) [25]. In addition, the heliothermal efficiency ($\eta_{heliothermal}$) quantifies the ability of the absorber to convert incident radiation into heat, and it can be calculated by the ratio between the absorbed solar flux density minus the radiative thermal losses, and the concentrated solar incident flux, according to this equation [21]:

$$\eta_{heliothermal} = \alpha_s - \frac{\varepsilon(T)\cdot\sigma\left(T^4 - T_0^4\right)}{C\cdot I\cdot\eta_{opt}} \quad (4)$$

where ε is the thermal emittance obtained at a working temperature of 270 °C and using the Plank's law, attaining ε value of 91 %, σ is the Stefan-Boltzmann constant, and T (270 °C) and T_0 (25 °C) are the receiver and ambient temperatures, respectively. The rest of the parameters are given of a typical concentrated solar linear technology. In particular, C and I relate to the solar concentration ratio (100) and to the incident solar flux density (900 W m^{-2}), respectively, and η_{opt} is the concentrator solar efficiency (0.8) [26]. In the case of 3DTES-SS, $\eta_{heliothermal}$ reached a value of 73 % that is suitable for CSP applications, especially when considering the added-value of storage in the PCM.

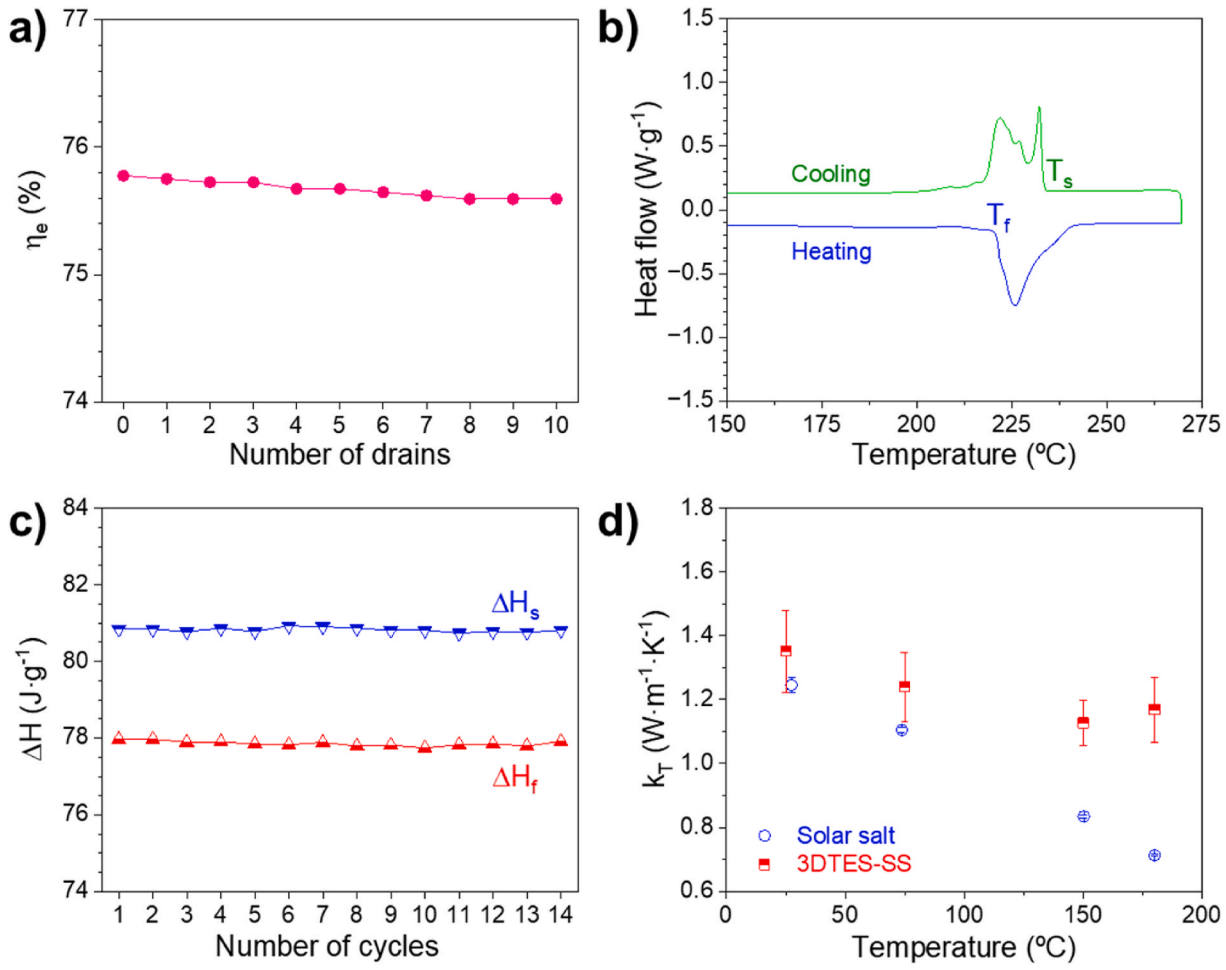

Fig. 4. Encapsulation and thermal characterization of 3DTES-SS. a) Encapsulation capacity (η_e) versus the number of drains of the infiltrated 3D AC_{ox}/Al_2O_3 supports, b) heating and cooling DSC curves of the 3DTES-SS, c) thermal cycling performance showing the evolution of the enthalpies of fusion (ΔH_f) and solidification (ΔH_s) with the number of thermal cycles, and d) thermal conductivity (k_T) of the solar salt and the 3DTES-SS as a function of the temperature.

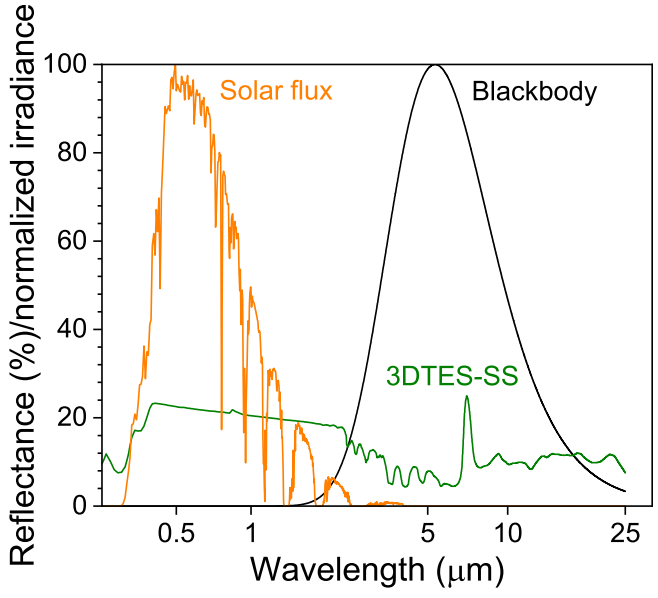

Fig. 5. Spectral reflectance spectra for the 3DTES-SS, solar flux and blackbody at 270 °C.

Finally, the mechanical strength of 3DTES-SS was analysed, taking into account that this parameter can be critical when using these FSPCMs under demanding operating conditions. From the strain-stress curves (see a representative example in Figure S3a), a σ_c value of 89.4 ± 3.6 MPa (strain of 24.1 ± 0.5 %) was calculated, which confirms the excellent mechanical response of 3DTES-SS, in line with other porous architectures infiltrated with molten salts, such as 3D printed clay supports infiltrated with sodium nitrate (σ_c = 68.0 MPa) [16] and alumina foams infiltrated with sodium sulphate (σ_c = 100.1 MPa) and sodium chloride (σ_c = 72.8 MPa) [11]. The compression tests also pointed the lack of catastrophic failure of 3DTES-SS. In the present work, the high compressive strength is mainly due to the contribution of the alumina (45 wt%) to the overall resistance of the printed skeleton. In fact, a σ_c value of 1.7 ± 0.2 MPa (strain of 5.5 ± 0.2 %) was obtained for the 3D AC_{ox}/Al_2O_3 support (Figure S3b), an improved mechanical response as compared to 3D clay supports (σ_c = 0.7 MPa) with similar patterned design and porosity [16].

4. Conclusions

Pseudoplastic aqueous AC_{ox}/boehmite inks have been direct ink written to build robust and highly porous (86 %) self-supported 3D AC_{ox}/Al_2O_3 scaffolds. The infiltration of these structures with molten solar salt have led to the development of novel TES materials with a good thermal energy storage efficiency (70 %). This response is due to the high encapsulation degree of the PCM into the open channels of the

scaffolds, which has been promoted by both the patterned design and the increasing wettability of the functionalized AC powders with the molten salt. The special configuration of the 3DTES-SS avoids the liquid leakage during the thermal cycling, keeping an excellent thermal stability as well. The thermal conductivity of the AC_{ox}/Al_2O_3 skeleton is the responsible for an increment of this parameter in the 3DTES-SS of up to 64 % (at 180 °C), leading to an energy storage density of 381 J g^{-1} in the operating temperature range of 25–270 °C. Besides, these TES materials also present an excellent absorbed energy capability ($\alpha_s = 79$ %) in the solar spectrum, which is mainly provided by the high solar absorptance of the 3D ceramic supports. This study points out the benefits of the direct ink writing technology as an excellent tool to develop novel materials with a promising energy storage performance for CSP applications.

CRediT authorship contribution statement

Irene Díaz-Herrezuelo: Writing – original draft, Validation, Methodology, Investigation, Formal analysis, Data curation. **Quentin Falcoz:** Writing – original draft, Methodology, Investigation, Formal analysis, Data curation. **Audrey Soum-Glaude:** Writing – original draft, Methodology, Investigation, Formal analysis, Data curation. **Manuel Belmonte:** Writing – original draft, Validation, Supervision, Resources, Project administration, Methodology, Investigation, Funding acquisition, Formal analysis, Conceptualization.

Declaration of competing interest

The authors declare that they have no known competing financial interests or personal relationships that could have appeared to influence the work reported in this paper.

Acknowledgements

This work was supported by the Grant PID2021-125427OB-I00 funded by MCIN/AEI/10.13039/501100011033 and by "ERDF A way of making Europe". This work was supported by the French "Investments for the future" program managed by the National Agency for Research under contract ANR-10-EQPX-49-SOCRATE. I. D.-H. is grateful to the JECS Trust for funding the visit to PROMES-CNRS laboratory (Contract No. 2023357). Authors thank C. Escape (PROMES-CNRS, UPR 8521) for his experimental assistance in the optical reflectance measurements.

Appendix A. Supplementary data

Supplementary data to this article can be found online at https://doi.org/10.1016/j.oceram.2024.100648.

References

[1] Y.B. Tao, Y.-L. He, A review of phase change material and performance enhancement method for latent heat storage system, Renew. Sustain. Energy Rev. 93 (2018) 245–259, https://doi.org/10.1016/j.rser.2018.05.028.
[2] N. Zhang, Y. Yuan, X. Cao, Y. Du, Z. Zhang, Y. Gui, Latent heat thermal energy storage systems with solid-liquid phase change materials: a review, Adv. Eng. Mater. 20 (2018) 1700753, https://doi.org/10.1002/adem.201700753.
[3] P. Liu, X. Chen, Y. Li, P. Cheng, Z. Tang, J. Lv, W. Aftab, G. Wang, Aerogels meet phase change materials: fundamentals, advances, and beyond, ACS Nano 16 (2022) 15586–15626, https://doi.org/10.1021/acsnano.2c05067.
[4] K. Liu, Z.F. Yuan, H.X. Zhao, C.H. Shi, F. Zhao, Properties and applications of shape-stabilized phase change energy storage materials based on porous material support - a review, Mater. Today Sustain. 21 (2023) 100336, https://doi.org/10.1016/j.mtsust.2023.100336.
[5] A. Islam, A.K. Pandey, R. Saidur, B. Aljafari, V.V. Tyagi, Advancements in foam-based phase change materials: unveiling leakage control, enhanced thermal conductivity, and promising applications, J. Energy Storage 74 (2023) 109380, https://doi.org/10.1016/j.est.2023.109380.
[6] T. Kim, D.M. France, W. Yu, W. Zhao, D. Singh, Heat transfer analysis of a latent heat thermal energy storage system using graphite foam for concentrated solar power, Sol. Energy 103 (2014) 438–447, https://doi.org/10.1016/j.solener.2014.02.038.
[7] D. Singh, T. Kim, W. Zhao, W. Yu, D.M. France, Development of graphite foam infiltrated with $MgCl_2$ for a latent heat based thermal energy storage (LHTES) system, Renew. Energy 94 (2016) 660–667, https://doi.org/10.1016/j.renene.2016.03.090.
[8] W. Zhao, D.M. France, W. Yu, T. Kim, D. Singh, Phase change material with graphite foam for applications in high-temperature latent heat storage systems of concentrated solar power plants, Renew. Energy 69 (2014) 134–146, https://doi.org/10.1016/j.renene.2014.03.031.
[9] H. Lan, S. Dutta, N. Vahedi, S. Neti, C.E. Romero, A. Oztekin, M. Nappa, R. Ruales, Graphite foam infiltration with mixed chloride salts as PCM for high-temperature latent heat storage applications, Sol. Energy 209 (2020) 505–514, https://doi.org/10.1016/j.solener.2020.09.029.
[10] P. Gimenez, A. Jove, C. Prieto, S. Fereres, Effect of an increased thermal contact resistance in a salt PCM-graphite foam composite TES system, Renew. Energy 106 (2017) 321–334, https://doi.org/10.1016/j.renene.2017.01.032.
[11] Z. Cai, Y. Li, S. Li, H. Wu, C. Bai, J. Tan, X. Xu, Y. Yin, W. Wang, Novel high thermal conductivity alumina/salt composites for thermal energy storage: effect of wettability on microstructure and properties, J. Eur. Ceram. Soc. 44 (2024) 3953–3964, https://doi.org/10.1016/j.jeurceramsoc.2024.01.063.
[12] Y. Li, J. Li, W. Feng, X. Wang, H. Nian, Design and preparation of the phase change materials paraffin/porous Al_2O_3@graphite foams with enhanced heat storage capacity and thermal conductivity, ACS Sustainable Chem. Eng. 5 (2017) 7594–7603, https://doi.org/10.1021/acssuschemeng.7b00889.
[13] S. Gong, X. Cheng, Y. Li, D. Shi, X. Wang, H. Zhong, Enhancement of ceramic foam modified hierarchical Al_2O_3@expanded graphite on thermal properties of 1-octadecanol phase change materials, J. Energy Storage 26 (2019) 101025, https://doi.org/10.1016/j.est.2019.101025.
[14] T.B. Freeman, K.E.O. Foster, C.J. Troxler, C.W. Irvin, A. Aday, S.K.S. Boetcher, A. Mahvi, M.K. Smith, A. Odukomaiya, Advanced materials and additive manufacturing for phase change thermal energy storage and management: a review, Adv. Energy Mater. 13 (2023) 2204208, https://doi.org/10.1002/aenm.202204208.
[15] S.A. Khan, M.A. Rahman, M. Khraisheh, I.G. Hassan, Advances in 3D printed periodic lattice structures for energy research: energy storage, transport and conversion applications, Mater. Des. 239 (2024) 112773, https://doi.org/10.1016/j.matdes.2024.112773.
[16] I. Diaz-Herrezuelo, L. Moreno-Sanabria, P. Miranzo, M.I. Osendi, M. Belmonte, Novel 3D thermal energy storage materials based on highly porous patterned printed clay supports infiltrated with molten nitrate salts, Addit. Manuf. 59 (2022) 103108, https://doi.org/10.1016/j.addma.2022.103108.
[17] I. Diaz-Herrezuelo, P. Miranzo, M.I. Osendi, M. Belmonte, High thermal energy storage efficiency of molten salts fully encapsulated into additive manufactured cellular vermiculite scaffolds, J. Energy Storage 85 (2024) 111108, https://doi.org/10.1016/j.est.2024.111108.
[18] A. Anagnostopoulos, H. Navarro, A. Alexiadis, Y. Ding, Wettability of $NaNO_3$ and KNO_3 on MgO and carbon surfaces - understanding the substrate and the length scale effects, J. Phys. Chem. C 124 (2020) 8140–8152, https://doi.org/10.1021/acs.jpcc.0c00978.
[19] K. Dujearic-Stephane, M. Gupta, A. Kumar, V. Sharma, S. Pandit, P. Bocchetta, Y. Kumar, The effect of modifications of activated carbon materials on the capacitive performance: surface, microstructure, and wettability, J. Compos. Sci. 5 (2021) 66, https://doi.org/10.3390/jcs5030066.
[20] https://www.nrel.gov/grid/solar-resource/spectra.html. (Accessed 6 June 2024).
[21] A. Soum-Glaude, A.L. Gal, M. Bichotte, C. Escape, L. Dubost, Optical characterization of $TiAlN_x/TiAlN_y/Al_2O_3$ tandem solar selective absorber coatings, Sol. Energy Mater. Sol. Cell. 170 (2017) 254–262, https://doi.org/10.1016/j.solmat.2017.06.007.
[22] T. Bauer, N. Pfleger, N. Breidenbach, M. Eck, D. Laing, S. Kaesche, Material aspects of solar salt for sensible heat storage, Appl. Energy 111 (2013) 1114–1119, https://doi.org/10.1016/j.apenergy.2013.04.072.
[23] S. Ma, Q. Yang, Y. Li, C. Yan, X. Wang, A review on preparation, thermal transport properties, phase-change characteristics, and thermal stability of molten salts, J. Clean. Prod. 444 (2024) 141272, https://doi.org/10.1016/j.jclepro.2024.141272.
[24] N.P. Siegel, M.D. Gross, R. Coury, The development of direct absorption and storage media for falling particle solar central receivers, J. Sol. Energy Eng. 137 (2015) 041003, https://doi.org/10.1115/1.4030069.
[25] X. Xu, S. Liu, Y. Liu, J. Wu, J. Yu, Y. Shen, Preparation and thermal shock resistance of solar thermal absorbing corundum ceramics for concentrated solar power, Int. J. Appl. Ceram. Technol. 21 (2023) 2102–2113, https://doi.org/10.1111/ijac.14700.
[26] A. Grosjean, A. Soum-Glaude, L. Thomas, Influence of operating conditions on the optical optimization of solar selective absorber coatings, Sol. Energy Mater. Sol. Cell. 230 (2021) 111280, https://doi.org/10.1016/j.solmat.2021.111280.